Rare Metals

ORIGINAL ARTICLE OPEN ACCESS

Continuous Stress Annealing Enables Ultralow-Loss Fe-Based Amorphous Alloys With Superior Magnetic Softness for Industrial Manufacturing

Zhi-Jun Guo[1] | Jun Li[1] | Jin-Hong Fu[1] | Ji-Feng Zhou[1] | Yan-Zhou Fan[1] | Xiao-Xuan Yang[1] | Ai-Na He[2] | Ya-Qiang Dong[2] | Qi-Kui Man[2] | Qiang Luo[1] | Bao-Long Shen[1]

[1]School of Materials Science and Engineering, Jiangsu Key Laboratory for Advanced Metallic Materials, Southeast University, Nanjing, China | [2]Zhejiang Province Key Laboratory of Magnetic Materials and Application Technology, CAS Key Laboratory of Magnetic Materials and Devices, Ningbo Institute of Materials Technology & Engineering, Chinese Academy of Sciences, Ningbo, China

Correspondence: Qiang Luo (q.luo@seu.edu.cn) | Bao-Long Shen (blshen@seu.edu.cn)

Received: 3 November 2025 | **Revised:** 16 January 2026 | **Accepted:** 19 January 2026

Keywords: continuous stress annealing | Fe-based amorphous soft magnetic alloys | magnetic anisotropy | magnetic domain evolution

ABSTRACT

Fe-based amorphous alloys are attractive soft magnetic materials for next-generation power electronics, yet simultaneously achieving high saturation magnetic flux density (B_s), low coercivity (H_c), and low core loss under scalable processing conditions remains challenging. Here, a composition–stress coupling strategy combining moderate Co substitution with optimized continuous stress annealing (CSA) is proposed to enhance magnetic performance and manufacturability. The optimized $Fe_{81.5-x}Co_xSi_{3.7}B_{14.5}C_{0.3}$ ($x = 1$) alloy is designed and exhibits outstanding properties, including low H_c of 0.92 A m^{-1}, high B_s of 1.65 T, ultralow core loss ($P_{10/50}$) of 0.031 W kg^{-1} at 1.0 T and 50 Hz, and an effective permeability (μ_e) of 12,200 at 1 A m^{-1} and 1 kHz. Compared with commercial Metglas 2605SA1, H_c and $P_{10/50}$ are reduced by 46% and 40%, respectively, whereas B_s is enhanced. Multiscale experiments and micromagnetic simulations reveal that optimal Co content and CSA induce medium-range atomic ordering and magnetoelastic coupling, generating robust uniaxial magnetic anisotropy and coherent three-dimensional magnetization. The CSA process offers a controllable, uniform, and energy-efficient route suitable for large-scale industrial production.

1 | Introduction

The demand for high-efficiency, compact, and low-loss power electronics has placed stringent requirements on soft magnetic materials. Conventional silicon steels, though widely used, suffer from high core loss and limited frequency capability. In contrast, Fe-based amorphous alloys, owing to their disordered atomic structures, exhibit high effective permeability (μ_e), low coercivity (H_c), and reduced core loss, making them strong candidates for next-generation high-efficiency power electronics, particularly in distribution transformers and high-power low-frequency inverters [1–3]. Their use in distribution transformers has significantly reduced transmission losses, whereas applications in electric vehicle motors have demonstrated a > 50% reduction in stator losses and notable noise suppression, highlighting their superiority over traditional materials. Nevertheless, a critical trade-off remains. Forming amorphous structures requires the addition of nonmagnetic elements, which lowers the saturation magnetic flux density (B_s) relative to silicon steels [4, 5]. The resulting reduction in B_s limits power density and hinders miniaturization of high-frequency components. Thus, reconciling high B_s with superior magnetic softness has become a central challenge in the design of Fe-based soft magnetic alloys.

Two main strategies have been explored to address this trade-off: composition design [6, 7] and postsolidification annealing

[8]. Increasing Fe content [9, 10] or partially substituting Fe with Co [11, 12] can enhance B_s, but these approaches introduce new trade-offs: reduced glass-forming ability at high Fe levels, whereas Co incorporation, although beneficial for B_s, tends to induce magnetic anisotropy and increase H_c when added beyond an optimal range [13–15]. Moreover, the high cost of Co limits its feasibility for large-scale industrial use. Therefore, optimized annealing remains essential to balance performance and economic practicality in Fe-based amorphous alloys.

Conventional normal annealing (NA) generally improves soft magnetic properties mainly by relieving internal stresses but may degrade magnetic performance in Co-containing Fe-based amorphous alloys [16]. Li et al. [17] discovered that NA has a detrimental effect on the magnetic performance of Fe-based amorphous alloys with high Co content. Alternatively, magnetic field annealing (FA) can enhance the soft magnetic performance of Co-rich Fe-based amorphous alloys. However, FA-induced magnetic anisotropy is relatively small because the controllable range of the composition and the intensity of the applied magnetic field are limited [18]. In addition, its efficacy diminishes near or above the Curie temperature (T_c) in low-Co or Co-free systems. Given the high cost of Co, developing annealing strategies compatible with low-Co and low-T_c alloys is of pressing importance. Stress annealing (SA) provides a promising solution by introducing tunable magnetic anisotropy independent of T_c. This technique enables precise modulation of both anisotropy magnitude and hysteresis loop shape, offering a powerful tool for tailoring soft magnetic behavior [1]. SA can be implemented in two modes: static stress annealing (SSA) and continuous stress annealing (CSA). Previous studies have shown that Metglas 2605HB1M amorphous alloy has low H_c and good mechanical toughness after SSA [19]. Additionally, SSA has been demonstrated to improve the soft magnetic performance of high-B_s Fe-based amorphous alloys [20]. Compared to SSA, CSA offers several advantages for large-scale continuous industrial processing. It enables uninterrupted operation, thereby improving production efficiency and throughput. Moreover, the uniform application of stress during CSA results in more consistent magnetic properties and enhanced quality control. Furthermore, CSA minimizes thermal cycling, conserves energy, and integrates seamlessly with automated in-line monitoring systems for real-time optimization, substantially reducing defects and costs. During CSA, a controlled/uniform tensile load is applied to the ribbons, which are continuously annealed and subsequently wound into transformer or inductor cores [21]. Thus, combining alloy composition tuning with CSA represents a compelling route toward realizing high-performance soft magnetic components for emerging power electronics. Recent reports have highlighted the efficacy of CSA in modulating anisotropy and enhancing magnetic performance. Zhu et al. [22] reported that CSA introduced controllable anisotropy in Finemet ribbons, enabling μ_e tuning from 413 to 1660. Zhang et al. [23] discovered that the application of stress during the annealing process has a significant impact on the electrical properties of nanocrystalline $Fe_{72.9}Si_{15.8}B_{6.9}Nb_{3.2}Cu_1Co_{0.2}$ material, specifically reducing its H_c and core loss by controlling the precipitation and growth of the α-Fe phase. Moreover, Kraus et al. [24] observed that the magnetic properties of $Co_{69}Fe_2Cr_7Si_8B_{14}$ ribbons were homogeneous along their length after CSA. However, its application to Fe-based amorphous systems, particularly for resolving the inherent trade-off between high B_s and low core loss at 1.0 T and 50 Hz ($P_{10/50}$), remains limited. In particular, the influence of CSA parameters, such as stress magnitude, annealing temperature (T_a), and process conditions, on stress-induced anisotropy (K_u), magnetic domain structure evolution, and soft magnetic performance in Fe-based amorphous alloys is not well understood.

Here, we demonstrate that CSA, when synergized with optimized Co substitution, provides a scalable pathway to ultralow-loss Fe-based amorphous alloys. Using $Fe_{81.5-x}Co_xSi_{3.7}B_{14.5}C_{0.3}$ ($x = 0$–8), we establish direct correlations among Co content, K_u, atomic ordering, domain structure, and macroscopic performance. Notably, the Co1 alloy subjected to CSA exhibits outstanding properties—low H_c (0.92 A m^{-1}), high B_s (1.65 T), ultralow $P_{10/50}$ (0.031 W kg^{-1}), and high μ_e (12,200 at 1 A m^{-1} and 1 kHz)—representing a 46% reduction in H_c and 40% lower loss compared with commercial Metglas 2605SA1. These findings reveal that moderate Co substitution synergizes with CSA to induce stress-assisted atomic ordering, K_u, and domain regularization, thereby unlocking superior soft magnetic properties. This study not only elucidates the mechanistic origin of stress–composition synergy in amorphous alloys but also establishes CSA as an exemplar for scalable processing of next-generation magnetic materials.

2 | Experimental

Alloy ingots with nominal compositions of $Fe_{81.5-x}Co_xSi_{3.7}B_{14.5}C_{0.3}$ ($x = 0, 1, 3, 4, 5, 6, 8$; denoted as Co0, Co1, Co3, Co4, Co5, Co6, and Co8) were synthesized by induction melting under argon protection using raw materials of Fe, Co, Si, B, and Fe-5 wt%C, all with a purity of at least 99.95 wt%. As-quenched (AQ) ribbons (~23 μm in thickness) were prepared by the single-roller melt-spinning technique. Subsequently, they were slit into 3.2 mm wide strips using a precision roll slitter. The custom-designed CSA apparatus features a feedback-controlled tensioning unit capable of real-time adjustment, maintaining stress fluctuations within 5%. Longitudinal stress was applied by controlled rotational differentials between the main and auxiliary pulleys. The heating furnace incorporated a high-efficiency heating component and multilayer insulation to ensure thermal uniformity. The effective heating zone length (L_e) was 0.6 m. At the optimized speed of 0.5 m min^{-1}, the effective annealing time (t_a) was 1.2 min. After passing through the heating zone, the ribbons were air-cooled to room temperature, whereas the applied tensile stress was maintained [25].

The microstructure of the ribbons was identified by X-ray diffraction (XRD, Bruker D8 DISCOVER) using Cu Kα radiation and high-resolution transmission electron microscopy (HRTEM, Talos F200X). Crystallization behaviors were investigated by differential scanning calorimetry (DSC, NETZSCH 404 F3) at a heating rate of 20°C min^{-1}. The B_s and initial magnetization curves for estimation of anisotropy energy were measured by a vibrating sample magnetometer (VSM, Lakeshore 7407). The H_c was evaluated by a DC B–H loop tracer (Riken BHS-40) with a maximum field of 1 kA m^{-1}. $P_{10/50}$ and μ_e were measured using an impedance analyzer (Keysight

E4990A) and an AC B–H loop tracer (Riken AC BH-100 K), respectively. The magnetic domain structure of the ribbons was observed using a magneto-optical Kerr microscope (evico magnetics, em-Kerr-Highres). Thermal expansion characteristics were assessed using a thermomechanical analyzer (TMA, NETZSCH 402 F3) under an argon atmosphere at a heating rate of 5°C min^{-1} with an applied stress of 0.05 N. To ensure statistical reliability, at least three samples were measured for each experimental condition. The reported results represent the mean values, with error bars indicating the standard deviations.

Micromagnetic simulations were performed using mumax3 to investigate the 3D magnetic domain configurations. The simulated geometry was 400 × 400 × 80 nm, with a unit cell size of 4 × 4 × 4 nm. Periodic boundary conditions were applied in the x and y directions (corresponding to the plane of the striped structure). The intrinsic magnetic parameters were set as follows: exchange stiffness constant $A = 5 \times 10^{-12}$ J m^{-1} and damping coefficient $\alpha = 0.01$. K_u was incorporated into the model, with its easy axis extending along the x-axis. The values for K_u were set to 12, 27, 641, and 379 J m^{-3} based on the experimental measurements of the Co1-AQ, Co1-NA, Co1-CSA, and Co8-CSA samples, respectively.

3 | Results and Discussion

3.1 | Optimization of CSA Process and Soft Magnetic Properties

XRD patterns confirm that all $Fe_{81.5-x}Co_xSi_{3.7}B_{14.5}C_{0.3}$ ribbons exhibit a fully amorphous structure, as proven by broad diffuse peaks (Supporting Information S1: Figure S1). The DSC analysis reveals two distinct exothermic peaks for each sample (Supporting Information S1: Figure S2), corresponding to successive crystallization events. The first peak and second peak correspond to the formation of α-Fe(Co) and hard magnetic Fe (Co)-B/C phase, respectively [26, 27]. With the increase of Co content, the first crystallization onset temperature (T_{x1}) gradually decreases from 496°C to 475°C, whereas the secondary temperature (T_{x2}) slightly increases from 529°C to 540°C. Consequently, the heat treatment window ($\Delta T_x = T_{x2}$-T_{x1}) broadens from 33°C to 65°C. This trend reflects a reduction in thermal stability, arising from the diminished fraction of metalloid elements with Co substitution. Furthermore, as the content of Co increases, T_c rises from 364°C to 450°C, which aligns with Narita's findings that the T_c of Co-doped alloys increases with higher Co content [28].

Thermal relaxation of the alloy occurs within 360°C–440°C, and all ribbons remain amorphous after CSA or NA. As shown in Supporting Information S1: Figures S3 and S4, CSA with 50 MPa stress consistently reduces H_c (Supporting Information S1: Figure S3A–G) and enhances μ_e compared to NA (Supporting Information S1: Figure S4A–G). For NA samples, the drop in H_c at 360°C–400°C arises from stress relaxation and free volume [29], which facilitate domain wall motion; at higher T_a, amorphous matrix densification and heterogeneous relaxation redistribute stress, hindering mobility and deteriorating the soft magnetic performance [30]. In contrast, CSA promotes atomic rearrangement and K_u formation, aligning magnetic domains along the stress axis and improving softness. At elevated T_a, however, stress-induced local ordering restricts domain wall motion [31], leading to reduced μ_e, higher H_c, and increased losses.

To optimize the running speed (i.e., the effective holding time) during the CSA of $Fe_{81.5-x}Co_xSi_{3.7}B_{14.5}C_{0.3}$ amorphous ribbons, running speeds of 0.1, 0.3, 0.5, 0.7, and 1 m min^{-1} were selected under a constant applied stress of 50 MPa. Figure 1A,B shows the variation of H_c and μ_e with running speed, respectively. All alloys (Co0–Co8) exhibit optimal soft magnetic properties at 0.5 m min^{-1}. This improvement arises because an appropriate annealing time enables domain reorganization, facilitating domain wall motion and thus enhancing magnetization-demagnetization processes [32]. At higher speeds, the shortened annealing time prevents sufficient free-volume relaxation and stress relief, deteriorating magnetic properties. Conversely, excessively slow speeds prolong annealing, causing over-relaxation and excessive atomic rearrangement. This promotes stress-driven localized enrichment of metalloid elements (e.g., B and Si), suppressing Fe–Co exchange interactions and ultimately deteriorating magnetic performance [33]. Based on the optimized running speed of 0.5 m min^{-1}, the influence of applied tensile stress was further examined by varying the stress from 0 to 150 MPa at optimal T_a. As shown in Figure 1C,D, both H_c and μ_e improve with increasing stress, reaching optimal performance at 50 MPa. At this level, residual stresses are effectively released, reducing magnetic domain wall pinning and enhancing magnetic softness [34]. At stresses below 50 MPa, residual internal stress is not sufficiently relieved, whereas excessive stress (> 50 MPa) generates strong stress gradients that destabilize the amorphous matrix and degrade properties [35]. Therefore, an applied stress of 50 MPa, combined with a running speed of 0.5 m min^{-1}, represents the optimum CSA condition for maximizing soft magnetic properties while ensuring compatibility with large-scale industrial processing. It is worth noting that although 0.5 m min^{-1} is used here, the process is industrially scalable. The required atomic relaxation time is constant; thus, industrial speeds (tens of m min^{-1}) can be achieved by proportionally increasing the L_e or optimizing t_a according to Equation (1).

$$v = \frac{L_e}{t_a} \tag{1}$$

This time–length equivalence provides a clear engineering pathway for translating the optimized CSA conditions established here to continuous, high-throughput industrial production lines.

The compositional dependence of magnetic performance in $Fe_{81.5-x}Co_xSi_{3.7}B_{14.5}C_{0.3}$ alloys reveals how the interplay between Co substitution and CSA governs soft magnetic behavior (Figure 2). With increasing Co content, H_c (Figure 2A) initially decreases and then rises, whereas μ_e (Figure 2B) exhibits the opposite trend, indicating that moderate Co addition combined with CSA markedly enhances magnetic softness. The synergistic effects of the thermal and stress fields are most pronounced in the Co1 alloy, which exhibits a 46% reduction in H_c compared with large-scale commercial Metglas 2605SA1 ($Fe_{80}Si_9B_{11}$) and

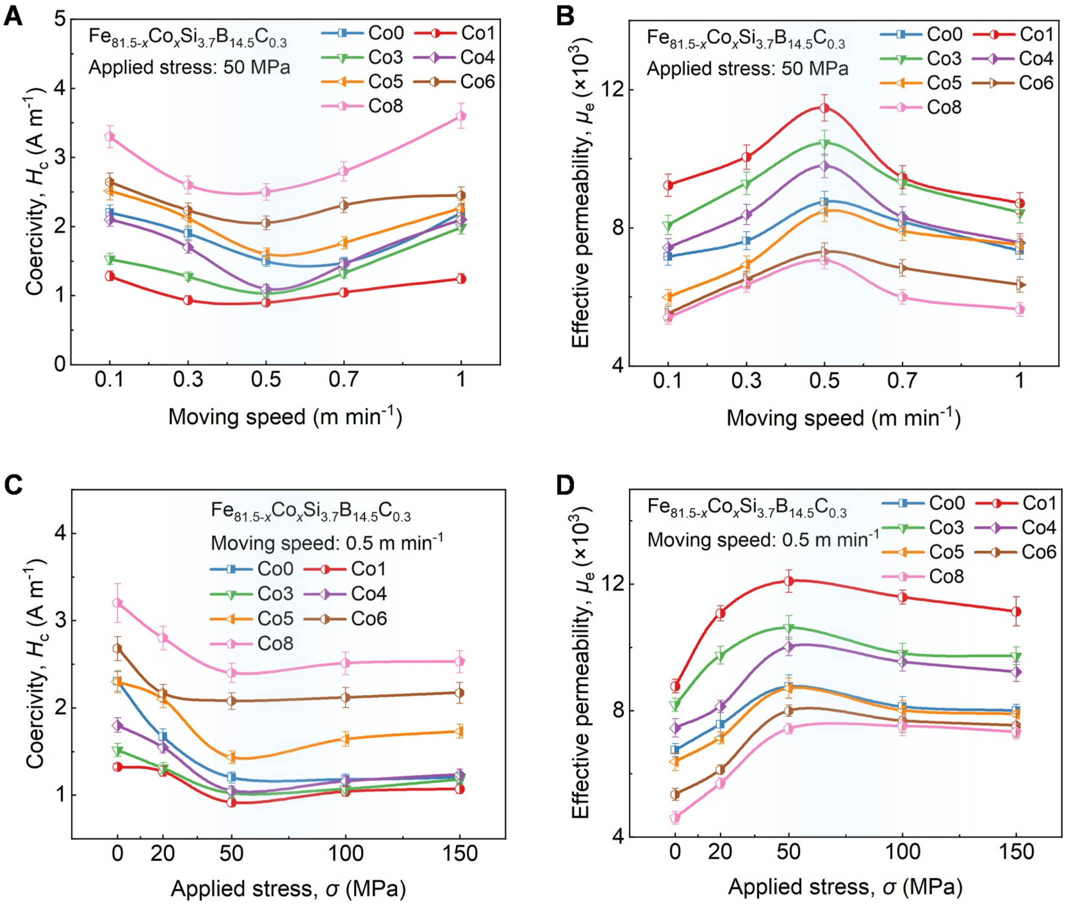

FIGURE 1 | Influence of CSA parameters on the soft magnetic properties of $Fe_{81.5-x}Co_xSi_{3.7}B_{14.5}C_{0.3}$ (x = 0, 1, 3, 4, 5, 6, 8) amorphous ribbons. (A) H_c and (B) μ_e as a function of moving speed under a constant applied stress of 50 MPa. (C) H_c and (D) μ_e as a function of applied stress at a constant moving speed of 0.5 m min^{-1}.

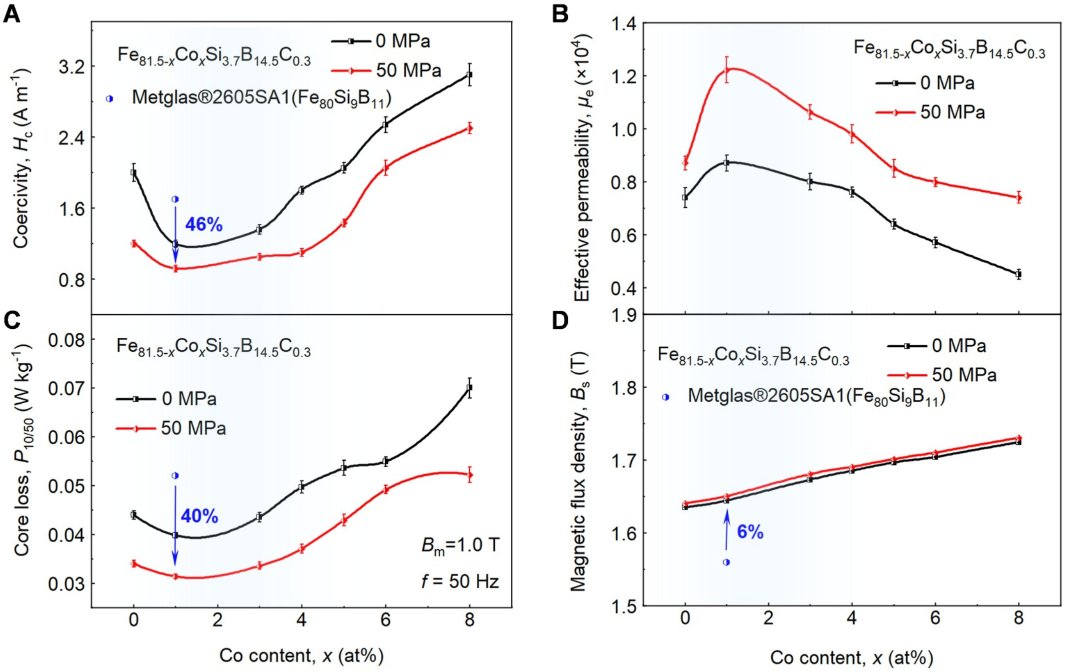

FIGURE 2 | Soft magnetic properties for $Fe_{81.5-x}Co_xSi_{3.7}B_{14.5}C_{0.3}$ alloys with varying Co contents after NA and CSA (50 MPa). Variations of (A) H_c, (B) μ_e, (C) $P_{10/50}$, and (D) B_s as a function of Co content (x).

delivers the best overall properties. As shown in Figure 2C, Co1-CSA (50 MPa) achieves an ultralow $P_{10/50}$ of 0.031 W kg^{-1}, representing a ~22% reduction relative to the NA sample and a 40% reduction compared to Metglas 2605SA1. Meanwhile, B_s (Figure 2D) increases from 1.64 to 1.73 T as Co content rises. According to the magnetic valence theory [36], Co addition enhances the average value of the magnetic moment of atoms in the amorphous phase, promoting a transition from weak to strong magnetism. In addition, Bethe Slater curves suggest that Co strengthens ferromagnetic exchange coupling between Fe-Co and Co-Co pairs, further contributing to the B_s enhancement [37]. Figure 3 benchmarks the B_s and $P_{10/50}$ values of representative soft magnetic alloys in the literature [38–46]. The CSA-optimized alloys developed in this work simultaneously achieve a high B_s (1.65 T) and an ultralow $P_{10/50}$ (0.031 W kg^{-1}), significantly outperforming most Fe-based soft magnetic alloys. In particular, they surpass conventional FeB- and FeCu-metalloid amorphous alloys in both B_s and $P_{10/50}$ while also exhibiting comparable or superior properties to FeCo-based nanocrystalline systems that typically require complex multi-stage heat treatments. From an industrial perspective, magnetic performance must be evaluated alongside economic feasibility, especially given the high cost of Co. In this regard, the present results demonstrate that low-level Co substitution (1 at%) offers a highly favorable cost–performance balance when coupled with CSA. Compared with the Co-free alloy processed under identical CSA conditions, the Co1 alloy exhibits a comprehensive enhancement in magnetic properties, including an approximately 9% reduction in power-frequency core loss ($P_{10/50}$) (from 0.034 to 0.031 W kg^{-1}), a 23% decrease in H_c (from 1.2 to 0.92 A m^{-1}), and a 35% increase in μ_e (from 9000 to 12,200). Over the decades-long service lifetime of distribution transformers, even a single-digit percentage reduction in core loss translates into substantial cumulative energy savings, which can effectively offset the marginal increase in raw material cost associated with low-level Co substitution. Moreover, the enhanced B_s enables core miniaturization, thereby reducing copper usage and overall device volume. Importantly, these benefits are achieved without resorting to high Co contents, which are known to significantly increase material cost and degrade stress-induced relaxation efficiency. Therefore, the present Co1–CSA strategy represents a practically viable and economically rational route for advancing high-performance Fe-based amorphous soft magnetic materials toward large-scale industrial deployment (Table 1).

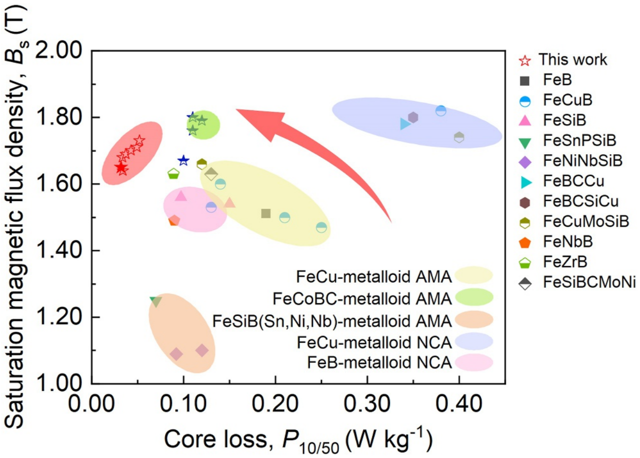

FIGURE 3 | Benchmark comparison of B_s and $P_{10/50}$ for representative soft magnetic alloys [38–46].

3.2 | Evolution of Magnetic Domain Structure and Dynamic Magnetization Behavior

Bridging the compositional and macroscopic property evolution, the magnetic domain morphology provides direct insight into how CSA and Co content jointly tune magnetic anisotropy (Figure 4 and Supporting Information S1: Figure S5). In the AQ state, the alloy displays arc-shaped strip domains coexisting with maze-like narrow domains, accompanied by abundant pinning sites arising from local magnetic anisotropy. These features reflect the coexistence of in-plane magnetic anisotropy [25] and perpendicular magnetic anisotropy [47], induced by magnetoelastic interactions associated with residual strain and local magnetostriction [48]. After NA, alloys with Co contents up to Co6 evolve into well-defined striped domains, whereas fingerprint-like morphologies disappear, confirming that annealing relieves internal stress via structural relaxation. In contrast, the Co8 sample retains domain structures with sharp edges and persistent branches, indicating strong pinning. This anomaly originates from excessive Co addition, which elevates T_c and causes T_a to lie far below T_c. Under such conditions, the alloy remains ferromagnetic rather than paramagnetic, preventing effective alignment of disordered magnetic moments [20]. This stabilizes local magnetic anisotropy, fixes domain walls, and complicates magnetic domain patterns. Under CSA at 50 MPa, all alloys exhibit highly oriented wide strip domains (> 250 μm) with straight, smooth walls, demonstrating effective suppression of domain wall pinning. Notably, Co1 exhibits the most uniform domain widths and smoothest domain walls. At higher Co contents, wide strip domains are also observed; however, their walls are irregular, with sharp edges and branching that reflect residual pinning effects. These observations demonstrate that the synergy between moderate Co substitution and applied stress promotes domain regularization, directly underpinning the enhanced softness achieved in the Co1 alloy.

TABLE 1 | Comparison of soft magnetic properties between current work and previous Fe-based amorphous alloys.

Alloys	H_c (A m^{-1})	μ_e (1 A m^{-1}, 1 kHz)	B_s (T)	$P_{10/50}$ (W kg^{-1})
$Fe_{80.5}Co_1Si_{3.7}B_{14.5}C_{0.3}$	0.92	12200	1.65	0.031
1K101 ($Fe_{91.7}Si_{5.3}B_{3.0}$)	2	9500	1.56	0.05
Metglas 2605SA1 ($Fe_{80}Si_9B_{11}$)	1.7	—	1.56	0.052
Metglas 2605HB1M ($Fe_{82–95}Si_{5–10}B_{1–5}$)	0.9	—	1.63	0.05

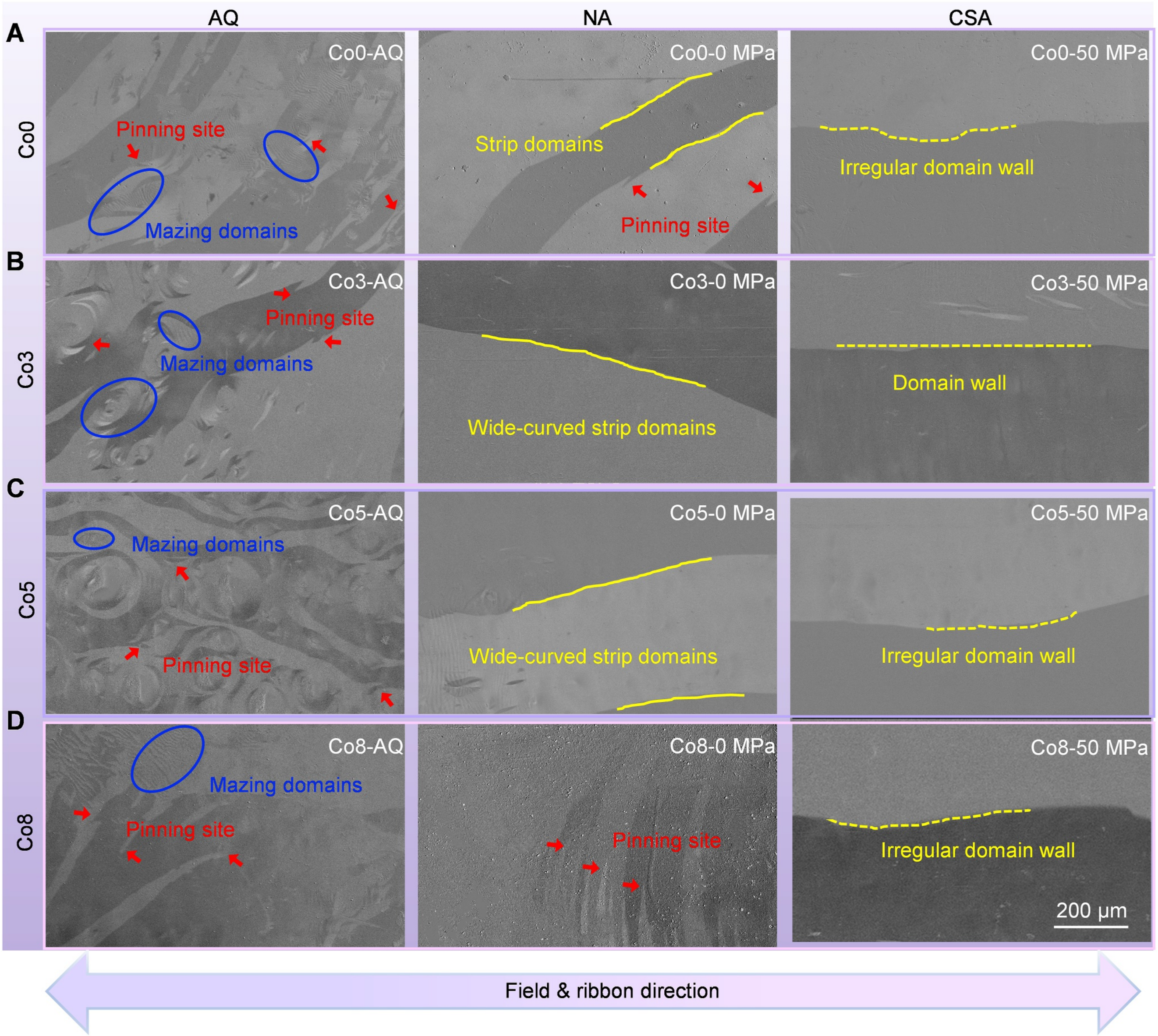

FIGURE 4 | Magnetic domain structures of demagnetized ribbons with different Co contents under different processing states. (A) Co0, (B) Co3, (C) Co5, and (D) Co8 in AQ, NA (0 MPa, 0.5 m min^{-1}), and CSA (50 MPa, 0.5 m min^{-1}) states.

Magnetization process imaging of the Co1 alloy under varying fields (Figure 5) further clarifies the role of CSA in domain wall dynamics. In the AQ state, wide planar domains coexist with fingerprint-like narrow domains that nucleate during early demagnetization. Reverse magnetization requires relatively high fields to reach saturation, with the process governed by a combination of domain wall displacement and magnetization rotation [49]. In the NA state, as the field changes, the domain wall moves irregularly and remains pinned at numerous local anisotropy pinning sites. These pinned regions hinder wall detachment and expansion, thereby restricting domain growth and slowing the reversal processes [50]. In sharp contrast, CSA-treated samples exhibit rapid, unobstructed domain wall displacement. Domains expand smoothly under the applied field, confirming that CSA effectively suppresses pinning, minimizes anisotropy fluctuations, and promotes efficient magnetization reversal. This enhanced domain wall mobility under CSA directly correlates with the superior soft magnetic properties of Co1.

The dynamic evolution of magnetic domains under optimal CSA conditions (50 MPa, 0.5 m min^{-1}) was further investigated for alloys with different Co contents (Figure 6 and Supporting Information S1: Figure S6). All samples display regularly aligned domains oriented along the ribbon's longitudinal axis. As the external field increases, the magnetization process is primarily governed by domain wall displacement. Domain walls move rapidly, and domains expand perpendicular to the ribbon axis. To quantify this dynamic behavior, domain wall displacements were measured as the applied magnetic field increased from 0 to 800 A m^{-1}. To ensure accuracy and eliminate nonuniformity caused by local pinning, measurements were taken at five different points along the domain wall and averaged. The resulting displacements are 273, 350, 316, 300, 260, 240, and 160 μm for Co0, Co1, Co3, Co4, Co5, Co6, and Co8, respectively. A comprehensive summary of the domain characteristics is provided in Table 2, including the demagnetized domain width, domain

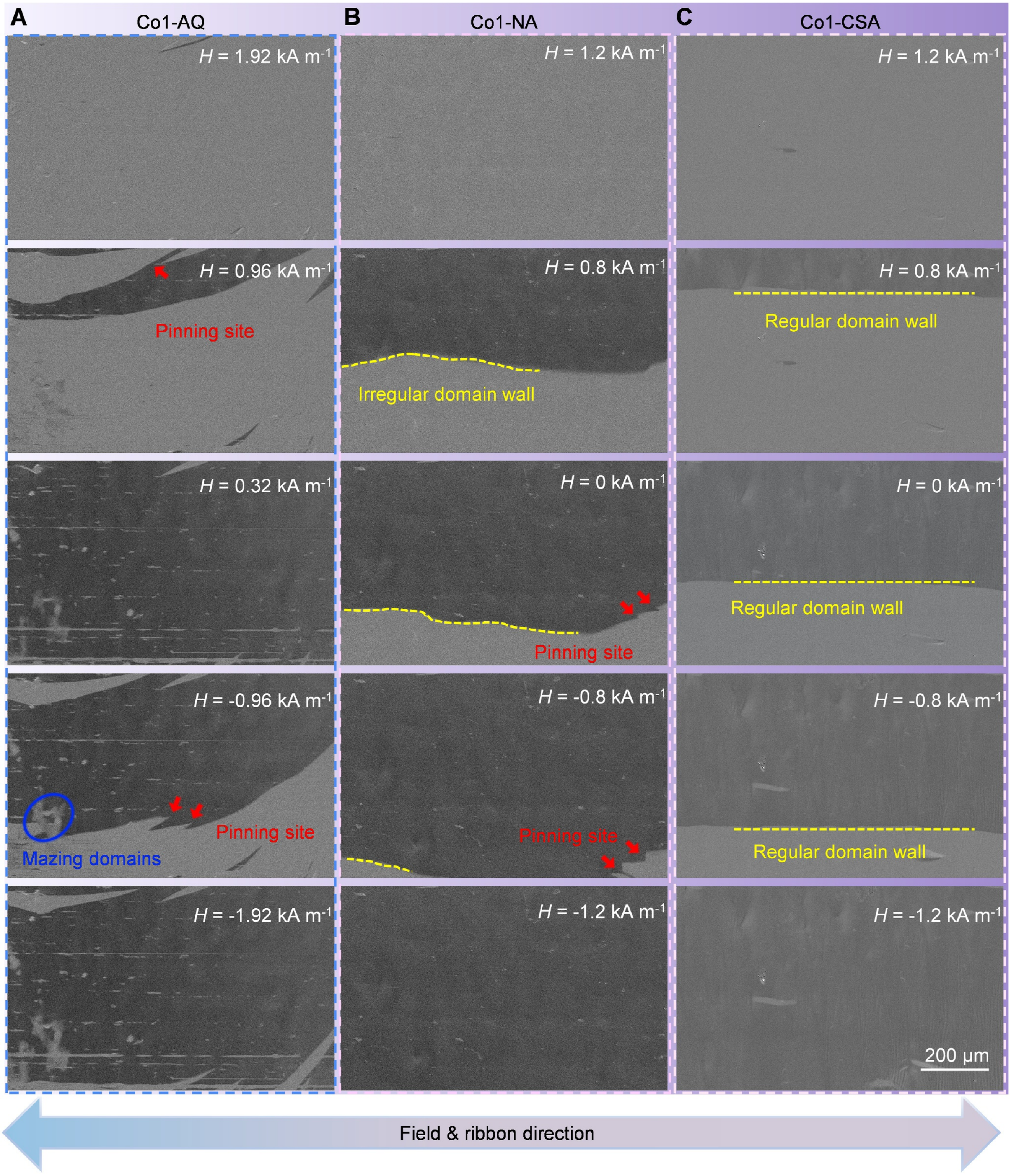

FIGURE 5 | Dynamic evolution of magnetic domains during the magnetization process for the Co1 alloy. (A) AQ state. (B) NA state (0 MPa, 0.5 m min^{-1}). (C) CSA state (50 MPa, 0.5 m min^{-1}).

wall tortuosity (defined as the ratio of the actual domain wall length to the linear end-to-end distance), and the domain wall displacement from 0 to 800 A m^{-1}. Among all compositions, the Co1 alloy exhibits the most uniform domain width and smoothest domain walls (lowest tortuosity), as well as the largest displacement response. These features indicate exceptionally smooth and mobile domain walls, reflecting the effective suppression of internal pinning sites through the synergistic coupling of moderate Co substitution and CSA. This optimized domain wall mobility provides a direct microscopic origin for the superior soft magnetic performance observed in the Co1 alloy.

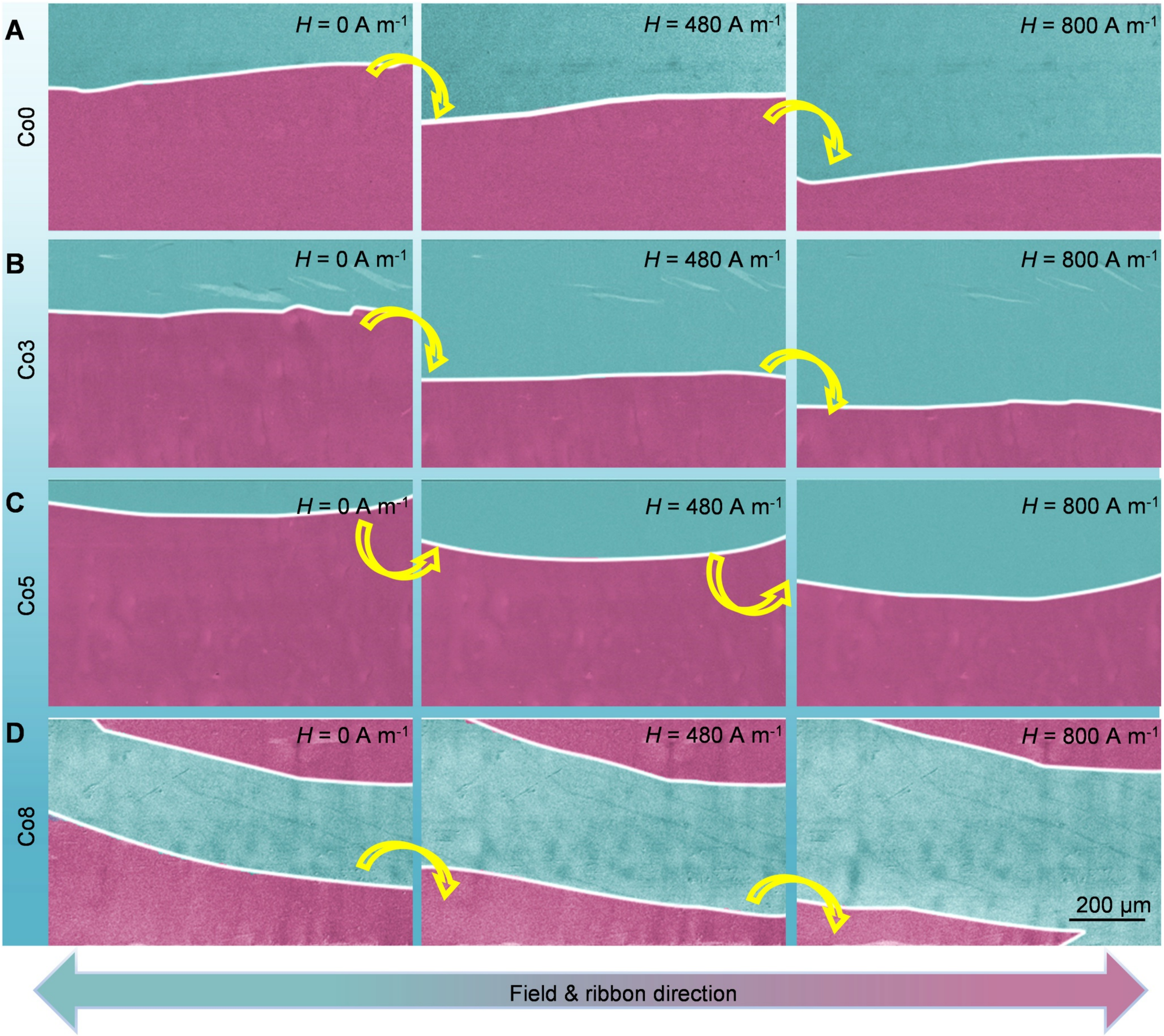

FIGURE 6 | Magnetic domain wall motion during magnetization for alloys subjected to the optimal CSA state (50 MPa, 0.5 m min^{-1}). (A) Co0. (B) Co3. (C) Co5. (D) Co8.

TABLE 2 | Summary of magnetic domain characteristics and domain wall displacements for Co0–Co8 alloys under the CSA state.

Sample	Domain width (μm)	Domain wall tortuosity	Displacement under 0–800 A m^{-1} field (μm)
Co0-CSA	250–290	1.043	273
Co1-CSA	310	1.001	350
Co3-CSA	240–260	1.015	316
Co4-CSA	250–330	1.033	300
Co5-CSA	240–340	1.038	260
Co6-CSA	230–290	1.046	240
Co8-CSA	220–260	1.121	160

3.3 | Mechanism of Stress-Induced Anisotropy and Theoretical Verification

The microstructural origin of the CSA-induced magnetic enhancement was further clarified through HRTEM and atomic ordering analyses of the Co1 and Co8 alloys (Figure 7). For the Co1 alloy in the AQ state (Figure 7A), diffuse amorphous scattering rings and disordered maze-like contrast dominate the image, with only ~3% of the analyzed region exhibiting local ordering. Subsequent NA (Figure 7B) slightly increases the

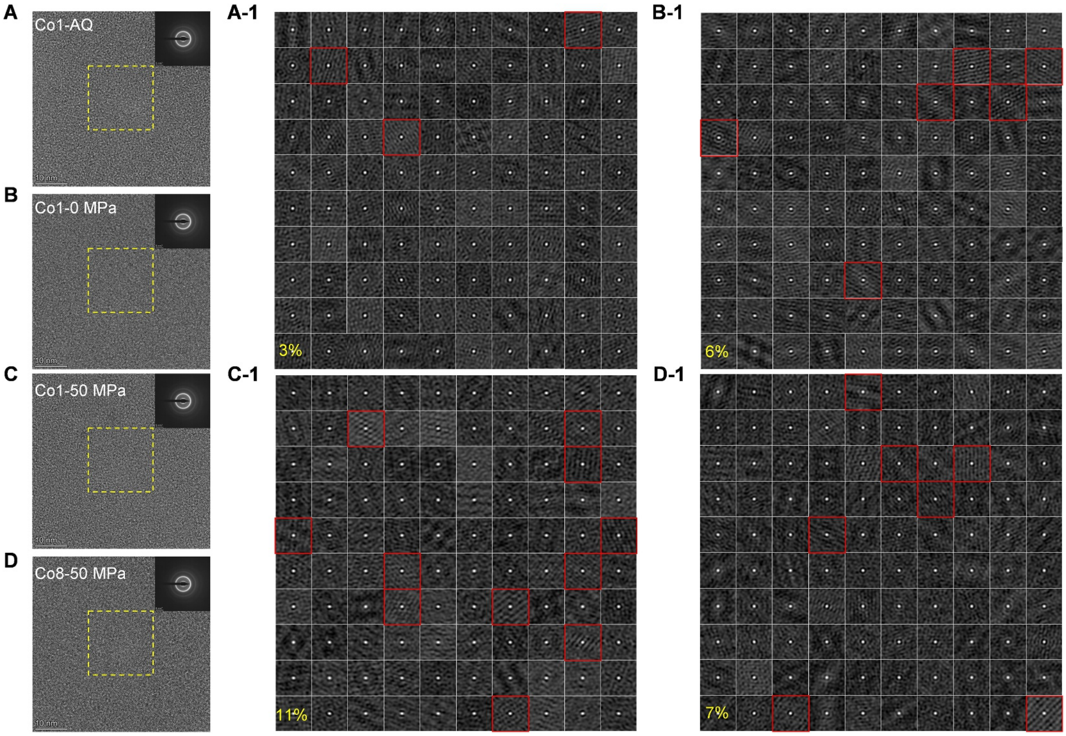

FIGURE 7 | HRTEM analysis of the local atomic structure and ordering. HRTEM images, selected area electron diffraction (SAED) patterns, and autocorrelation analysis for (A) Co1-AQ, (B) Co1-NA (0 MPa, 0.5 m min^{-1}), (C) Co1-CSA (50 MPa, 0.5 m min^{-1}), and (D) Co8-CSA (50 MPa, 0.5 m min^{-1}) samples, with ordered fractions indicated in yellow.

ordered fraction to 6%, indicating slight growth of locally crystalline structures within the amorphous matrix [51]. In contrast, CSA at 50 MPa (Figure 7C) markedly raises the ordered fraction to ~11%. To ensure statistical representativeness, HRTEM analyses were conducted on at least five randomly selected regions for each sample. For the Co1-CSA alloy, the average ordering degree was 11% with a standard deviation of ~0.4%, confirming the uniformity and reproducibility of the stress-induced structural ordering. This demonstrates that the applied stress field markedly enhances atomic mobility and lowers the activation diffusion barrier, thereby promoting a more regular atomic arrangement and higher medium-range order [52]. These results show the importance of external stress in driving stress-assisted ordering. For the Co8 alloy (Figure 7D), the ordered fraction reaches only ~7% under identical CSA conditions. This composition-dependent response indicates that excessive Co addition constrains atomic rearrangement, likely due to the higher magnetic exchange stiffness and elevated Curie temperature, which restrict stress-assisted diffusion. Consequently, Co1 displays the most pronounced ordering effect, establishing a direct microstructural foundation for its superior soft magnetic performance.

The magnetic anisotropy governing the observed domain evolution and microstructural response was quantitatively assessed by evaluating the intrinsic average anisotropy constant ($< K >$) and K_u for Co0-8 alloys subjected to NA and CSA (Figure 8 and Supporting Information S1: Figure S7). To determine the magnetic anisotropy field (H_k) and subsequently calculate K_u, hysteresis loops were measured along the transverse direction of the ribbons, followed by a demagnetization correction. The demagnetization factor (N_D) can be calculated using Equation (2) [53]:

$$1/\chi^* = \left(\mathrm{d}M/\mathrm{d}H_\mathrm{app}\right)^{-1} = 1/\chi + N_\mathrm{D} \tag{2}$$

where M is the magnetization, H_app is the applied magnetic field, and χ is the actual magnetic susceptibility. By analyzing the lower-limit value of the reciprocal technical susceptibility (χ^*), N_D was determined to be 5×10^{-3}. The effective magnetic field (H_eff) was then calculated using Equation (3):

$$H_\mathrm{eff} = H_\mathrm{app} - N_\mathrm{D} M \tag{3}$$

Finally, K_u was obtained using Equation (4) [54]:

$$K_\mathrm{u} = \frac{1}{2} H_\mathrm{k} B_\mathrm{s} \tag{4}$$

Compared with NA samples, CSA samples display more linear magnetization behavior, signifying the formation of a well-defined uniaxial magnetic anisotropy along the ribbon axis. Similar to field-annealed soft magnetic alloys [55], CSA introduces a longitudinal susceptibility axis through stress-induced strain, which couples with magnetization and aligns magnetic moments along the applied stress direction. As shown in Figure 8B, the Co1-CSA alloy exhibits the strongest uniaxial magnetic anisotropy, with K_u = 641 J m^{-3} and an H_k value of 801 A m^{-1}. The approximate proportionality between K_u and H_k across the compositions suggests effective orientation of local magnetic moments along the induced easy axis [56], forming wide magnetic domains aligned with the stress direction. Differences in K_u among compositions originate from the combined effects of Co content and structural relaxation. For Co1 alloys, a moderate Co substitution optimizes the local atomic environment, strengthening the magnetoelastic effect induced

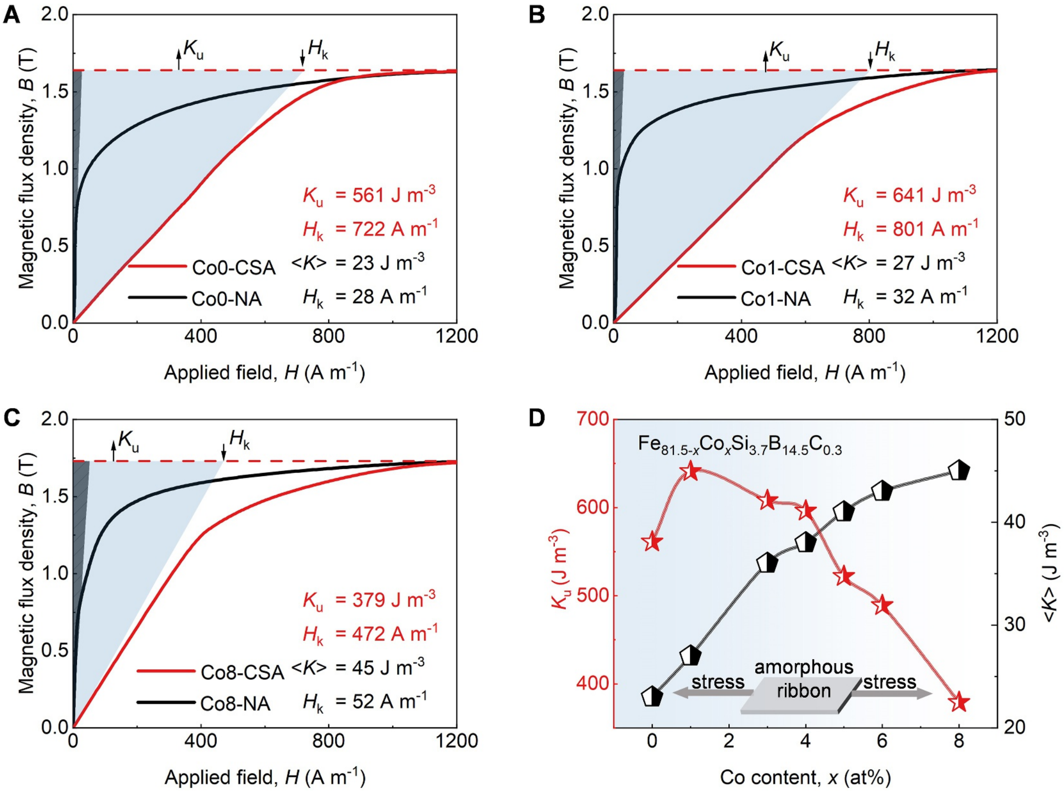

FIGURE 8 | Analysis of magnetic anisotropy induced by CSA and the correlation with Co content. Initial magnetization curves measured along the transverse direction and corrected for demagnetization for (A) Co0, (B) Co1, and (C) Co8 alloys. (D) Variation of K_u and $< K >$ with Co content.

by CSA. This effectively facilitates the alignment of magnetic moments along the stress direction, generates strong uniaxial magnetic anisotropy, and suppresses local magnetic inhomogeneity. By contrast, excessive Co (e.g., Co8 alloys) reduces the efficiency of stress-induced atomic rearrangement. HRTEM images (Figure 7) confirm that Co8-CSA exhibits a lower degree of medium-range order compared with Co1-CSA, indicating that excess Co modifies interatomic bonding and stabilizes configurations detrimental to soft magnetic behavior. Moreover, the elevated T_c of Co8 means that T_a lies far below T_c. Under such conditions, the system remains strongly ferromagnetic during annealing, preventing full relaxation of disordered domains. Consequently, irregular domain configurations persist, and $< K >$ remains relatively large. This highlights that $< K >$ is strongly composition-dependent: Although moderate Co addition enhances stress sensitivity and K_u, excessive Co elevates $< K >$, destabilizes domain structures, and ultimately degrades soft magnetic performance. Overall, annealing serves to release internal stresses, reduce free volume, and eliminate local inhomogeneities [57]. When balanced with a moderate Co substitution (Co1), CSA-applied stress, T_a, and running speed act synergistically to promote atomic rearrangement, enhance medium-range order, and generate robust uniaxial magnetic anisotropy. This stress–composition synergy enables Co1 to achieve the most outstanding soft magnetic properties across H_c, μ_e, $P_{10/50}$, and magnetic domain structure/stability.

The thermomechanical response of the Co1 alloy under optimized CSA provides direct evidence of stress-induced structural relaxation and its magnetoelastic origin (Supporting Information S1: Figure S8). The thermal expansion behavior can be divided into three characteristic regions: (I) from room temperature to T_1, both stress-free and stress-annealed samples exhibit typical linear thermal expansion; (II) between T_1 and T_2, a clear divergence emerges. The stress-free sample shows a reduced expansion rate due to densification induced by free-volume annihilation, whereas the CSA sample displays a more pronounced suppression of expansion, confirming the relaxation of tensile elastic strain introduced along the ribbon axis during annealing; (III) from T_2 to 540°C, both samples undergo initial expansion followed by abrupt shrinkage associated with crystallization. To quantify this effect, the temperature derivative of the strain difference ($\Delta\varepsilon$) was analyzed (inset of Supporting Information S1: Figure S8). A distinct peak appears near 400°C, coinciding precisely with the stress-annealing temperature, thereby revealing a thermal "memory effect" of the alloy system toward its original treatment condition. Integration of the peak yields a constrained elastic strain of ~0.22%, confirming that K_u originates from magnetoelastic effects [48, 58].

The preceding thermomechanical and structural analyses demonstrate that continuous stress annealing (CSA) induces pronounced magnetoelastic coupling that governs both microscopic ordering and macroscopic anisotropy. To consolidate these findings, Figure 9 schematically illustrates the multiscale mechanism of structural and magnetic evolution during CSA. At the atomic scale, the amorphous structure can be described by the flow-unit model proposed by Kozikowski et al. [58], in which a rigid elastic matrix is interspersed with locally soft

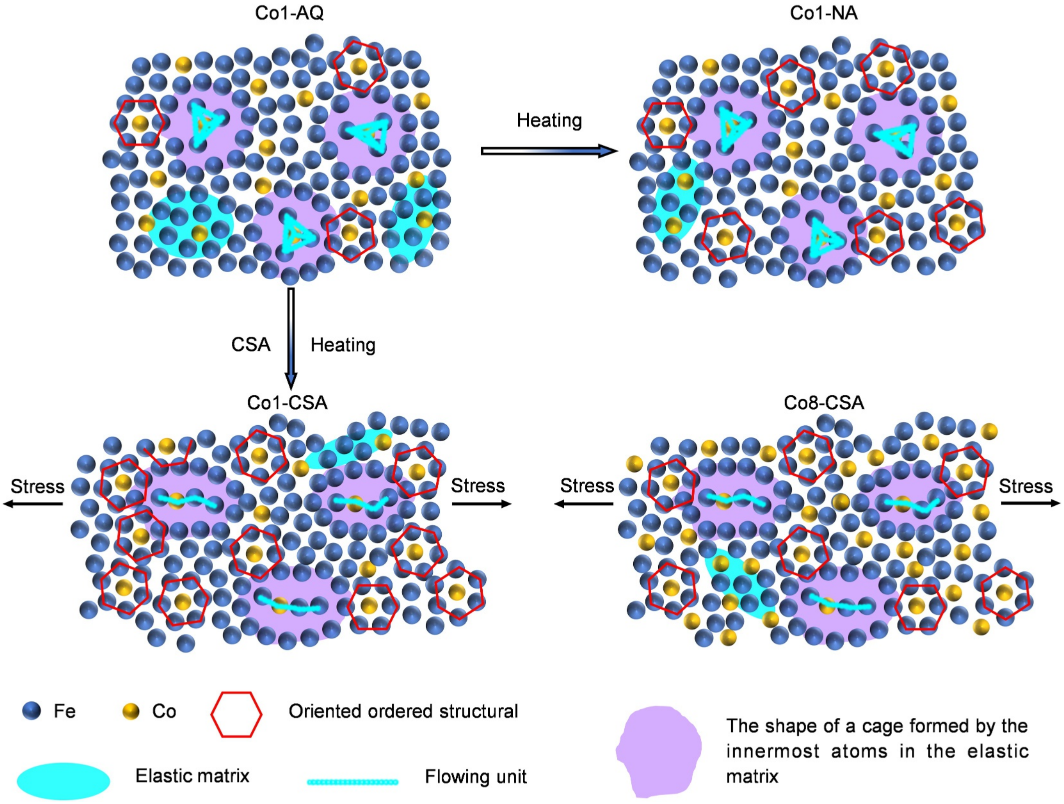

FIGURE 9 | Schematic illustration of the atomic-scale structural evolution and stress-induced anisotropy mechanism. Structural models for Co1-AQ, Co1-NA, Co1-CSA, and Co8-CSA, highlighting the rearrangement of flow units and the formation of oriented ordered motifs under stress.

"flow units" that behave in a liquid-like fashion and readily undergo shear rearrangement. As illustrated for Co1-CSA, the dense elastic matrix (cyan background) is elongated under applied tensile stress. The purple region represents the cage-like configurations formed by inner-shell atoms of the elastic matrix, typically encapsulating free-volume zones. At elevated temperatures, atoms in locally loose regions (cyan dashed line) exhibit high mobility and gradually diffuse or rearrange to adapt to the deformed cage, thereby releasing local elastic energy. In Co1-CSA, the applied tensile stress elongates the cage (purple regions), whereas loosely packed atoms inside the cage preferentially align along the stress axis, forming chain-like configurations. Upon cooling, these atoms are immobilized, preventing the cage from fully recovering to its original geometry. Consequently, a fraction of the elastic elongation remains stored as residual constrained strain [59]. This stress-induced atomic ordering (red hexagonal motifs) corresponds to the ordered regions observed in Figure 7. In contrast, Co1-AQ and Co1-NA exhibit isotropic random disorder, as they do not experience directional elastic deformation and cooperative atomic rearrangement. The degree of ordering is strongly composition-dependent. Excessive Co promotes magnetocrystalline anisotropy, as seen in Co8-CSA, where stress-induced ordering is suppressed and structural inhomogeneity persists, ultimately degrading soft magnetic properties.

Micromagnetic simulations were conducted to complement surface Kerr imaging and provide a three-dimensional perspective of the magnetization structure within the ribbons (Figure 10). The simulated results not only reproduce the experimentally observed surface domain morphologies but also unveil the internal magnetization distribution across the ribbon thickness. In the Co1-AQ state (Figure 10A), the magnetization vectors exhibit highly disordered orientations with vortex-like configurations. This disordered topology arises from heterogeneous internal stresses introduced during rapid solidification, which generate randomly distributed local anisotropy and strong pinning sites. After normal annealing (Co1-NA, Figure 10B), elongated stripe-like domains emerge. However, due to the isotropic nature of the relaxation in the absence of directional loading, broad transition regions persist. This indicates that magnetization alignment within the ribbon interior remains incomplete. By contrast, the cross-sectional views of Co1-CSA (Figure 10C) reveal a highly coherent magnetization structure, with magnetic moments uniformly aligned throughout the ribbon thickness. This provides direct three-dimensional evidence that tensile stress introduces uniaxial magnetic anisotropy, effectively suppressing internal pinning and enabling consistent magnetization alignment across the ribbon. Conversely, although macroscopic stripe domains are also observed on the surface of Co8-CSA (Figure 10D), the internal cross-sections expose distinct local distortions. These features arise from the excessive Co content, which increases intrinsic exchange stiffness and magnetocrystalline anisotropy, thereby inhibiting complete stress-assisted relaxation. Consequently, the elevated K_u (379 J m^{-3}) reflects persistent anisotropy inhomogeneity. Together, these 3D simulations confirm that optimized CSA establishes coherent magnetization, whereas excessive Co enrichment disrupts exchange uniformity and reintroduces pinning, thereby undermining magnetic softness.

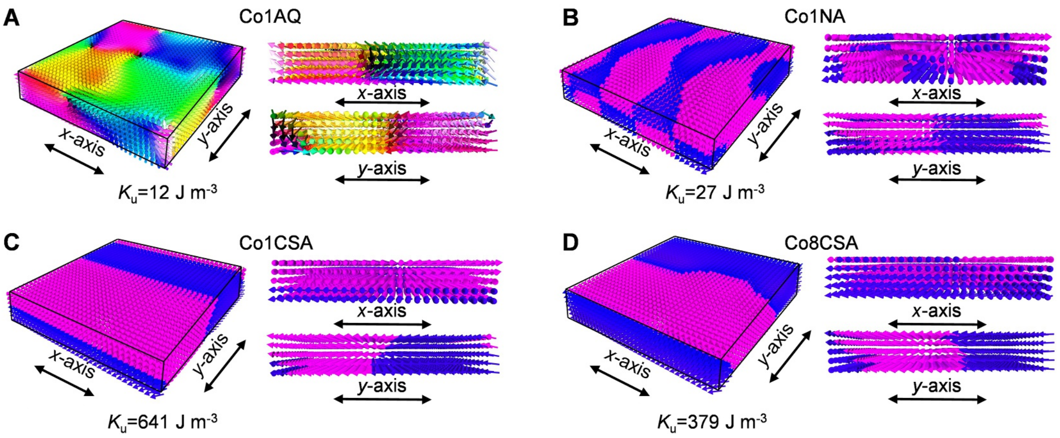

FIGURE 10 | Micromagnetic simulations of three-dimensional magnetic domain structures. 3D views and corresponding *x*–*z*/*y*–*z* cross-sectional profiles for (A) Co1-AQ, (B) Co1-NA, (C) Co1-CSA, and (D) Co8-CSA samples.

4 | Conclusions

This study presents a composition–stress coupling strategy that fundamentally advances the design of Fe-based amorphous soft magnetic alloys while offering direct industrial scalability. By integrating moderate Co substitution with a CSA process, the optimized $Fe_{81.5-x}Co_xSi_{3.7}B_{14.5}C_{0.3}$ ($x = 1$) alloy achieves an exceptional combination of ultralow H_c (0.92 A m^{-1}), high B_s (1.65 T), low $P_{10/50}$ (0.031 W kg^{-1}), and high μ_e (12200 at 1 A m^{-1}, 1 kHz), surpassing commercial Fe-based amorphous alloys such as Metglas 2605SA1. Multiscale analyses and micromagnetic simulations reveal that CSA induces medium-range atomic ordering and magnetoelastic coupling, where tensile stress promotes cooperative atomic rearrangement and the formation of chain-like ordered motifs that generate robust uniaxial magnetic anisotropy along the ribbon axis. This anisotropy yields wide, oriented magnetic domains with minimal pinning, drastically reducing hysteresis loss. In contrast, excessive Co addition increases exchange stiffness and intrinsic anisotropy, suppressing stress-assisted ordering and degrading softness. Unlike conventional stepwise stress annealing, CSA operates continuously under controllable tensile loads and temperatures, enabling uniform anisotropy induction and efficient internal stress relaxation in long ribbons—features that make it highly compatible with large-scale, high-throughput industrial production. Overall, this work establishes CSA-composition synergy as a transformative and scalable pathway for producing next-generation Fe-based amorphous alloys with low loss, high B_s, and outstanding performance for advanced power electronic devices.

Author Contributions

Zhi-Jun Guo: conceptualization, funding acquisition, investigation, methodology, supervision, writing – original draft, writing – review and editing. **Jun Li:** data curation, formal analysis, methodology, writing – original draft. **Jin-Hong Fu:** data curation, formal analysis. **Ji-Feng Zhou:** formal analysis, methodology. **Yan-Zhou Fan:** data curation, methodology. **Xiao-Xuan Yang:** data curation. **Ai-Na He:** methodology. **Ya-Qiang Dong:** methodology. **Qi-Kui Man:** methodology. **Qiang Luo:** conceptualization, funding acquisition, supervision, writing – review and editing. **Bao-Long Shen:** conceptualization, funding acquisition, project administration, supervision, writing – review and editing.

Acknowledgments

This study was financially supported by the National Natural Science Foundation of China (Grant No. 52231005), the National Key Research and Development Program of China (Grant No. 2022YFB3804100), the Science Technology Development Program of Yixing (Grant No. C2024002), the Start-up Research Fund of Southeast University (Grant No. RF1028623113), and the Natural Science Foundation of Jiangsu Province (Grant No. BK20221474). The authors thank the Center for Fundamental and Interdisciplinary Sciences of Southeast University for support in magnetic domain measurement.

Conflicts of Interest

The authors declare no conflicts of interest.

Data Availability Statement

The data that support the findings of this study are available from the corresponding author upon reasonable request.

References

1. G. Herzer, "Modern Soft Magnets: Amorphous and Nanocrystalline Materials," *Acta Materialia* 61, no. 3 (2013): 718–734, https://doi.org/10.1016/j.actamat.2012.10.040.

2. J. P. Qu, J. Liu, S. P. Yue, et al., "Optimization of Microstructure and Properties of Cu-Cr-Zr-Si Alloy by Rotating Magnetic Field," *Copper Engineering* 5 (2023): 1–9, https://doi.org/10.3969/j.issn.1009-3842.2023.05.001.

3. Y. Z. Fan, Z. J. Guo, M. Wang, et al., "Phosphating-Enhanced Fe-Based Amorphous Soft Magnetic Composites With Ultra-Low Power Loss for Efficient Electrical Energy Conversion," *Science China Physics, Mechanics & Astronomy* 68, no. 10 (2025): 106112, https://doi.org/10.1007/s11433-025-2711-2.

4. L. Hou, X. D. Fan, Q. Q. Wang, W. M. Yang, and B. L. Shen, "Microstructure and Soft-Magnetic Properties of FeCoPCCu Nanocrystalline Alloys," *Journal of Materials Science & Technology* 35, no. 8 (2019): 1655–1661, https://doi.org/10.1016/j.jmst.2019.03.030.

5. S. J. Kang, Z. Chen, Q. K. Zhu, K. W. Zhang, Z. H. Guo, and Z. J. Yan, "Microalloying and Pre-Annealing Co-Modulation of the Nanocrystalline Structure and Soft Magnetic Properties of Fe(Co)SiBPCu Alloys," *Rare Metals* 44, no. 9 (2025): 6547–6561, https://doi.org/10.1007/s12598-025-03312-z.

6. Y. S. Choi, D. H. Kwon, M. W. Lee, et al., "A Study on the Optimization of Metalloid Contents of Fe-Si-B-C Based Amorphous Soft Magnetic Materials Using Artificial Intelligence Method," *Archives of*

Metallurgy and Materials 67, no. 4 (2022): 1459–1463, https://doi.org/10.24425/amm.2022.141074.

7. Y. Z. Fan, C. L. Jin, M. Wang, et al., “Nb Microalloying Enhances the Amorphous Forming Ability and Soft Magnetic Properties of High B_s Fe-Based Nanocrystalline Alloys,” *Journal of Alloys and Compounds* 1044 (2025): 184627, https://doi.org/10.1016/j.jallcom.2025.184627.

8. C. C. Cao, L. Zhu, Y. Meng, X. B. Zhai, and Y. G. Wang, “Atomic Level Structural Modulation During the Structural Relaxation and Its Effect on Magnetic Properties of $Fe_{81}Si_4B_{10}P_4Cu_1$ Nanocrystalline Alloy,” *Journal of Magnetism and Magnetic Materials* 456 (2018): 274–280, https://doi.org/10.1016/j.jmmm.2018.02.043.

9. H. Li, A. D. Wang, T. Liu, et al., “Design of Fe-Based Nanocrystalline Alloys With Superior Magnetization and Manufacturability,” *Materials Today* 42 (2021): 49–56, https://doi.org/10.1016/j.mattod.2020.09.030.

10. A. D. Wang, C. L. Zhao, H. Men, et al., “Fe-Based Amorphous Alloys for Wide Ribbon Production With High B_s and Outstanding Amorphous Forming Ability,” *Journal of Alloys and Compounds* 630 (2015): 209–213, https://doi.org/10.1016/j.jallcom.2015.01.056.

11. Z. D. Li, W. W. Zhang, G. T. Li, et al., “Magnetic Field Annealing of FeCo-Based Amorphous Alloys to Enhance Thermal Stability and Curie Temperature,” *Rare Metals* 42, no. 6 (2023): 2000–2006, https://doi.org/10.1007/s12598-018-1069-z.

12. B. Fu, J. Han, S. Q. Guo, et al., “Room-Temperature and High-Temperature Magnetic Permeability of Co-Doped Nanocrystalline Alloys,” *Rare Metals* 37, no. 5 (2018): 427–432, https://doi.org/10.1007/s12598-018-1037-7.

13. A. Inoue, B. L. Shen, and C. T. Chang, “Super-High Strength of Over 4000 MPa for Fe-Based Bulk Glassy Alloys in $[(Fe_{1-x}Co_x)_{0.75}B_{0.2}Si_{0.05}]_{96}Nb_4$ System,” *Acta Materialia* 52, no. 14 (2004): 4093–4099, https://doi.org/10.1016/j.actamat.2004.05.022.

14. M. F. Jiang, J. J. Wang, M. J. Cai, et al., “Improvement of Soft Magnetic Properties for Fe-Based Amorphous/Nanocrystalline Alloy by Longitudinal Magnetic Field Annealing,” *Journal of Non-Crystalline Solids* 650 (2025): 123382, https://doi.org/10.1016/j.jnoncrysol.2024.123382.

15. M. J. Cai, Z. J. Guo, L. Li, et al., “Obtaining Extremely Low Coercivity of High B_s FeCoBSiCPCu Nanocrystalline Alloys Through Modulation of Magnetic Anisotropy,” *Journal of Materials Science & Technology* 207 (2025): 105–112, https://doi.org/10.1016/j.jmst.2024.04.047.

16. B. J. Ma, Q. Ma, Y. L. Liu, et al., “Interface Control and Magnetic Circuit Simulation of Fe-Co Gradient Soft Magnetic Materials,” *Chinese Journal of Rare Metals* 49, no. 4 (2025): 518–527, https://doi.org/10.13373/j.cnki.cjrm.XY21040005.

17. Z. Li, H. M. Hu, S. Y. Shi, et al., “Enhanced Soft Magnetic Properties of FeCoBSiCu Amorphous Alloys by Confined α-Fe(Co) Nanophase,” *Journal of Non-Crystalline Solids* 640 (2024): 123130, https://doi.org/10.1016/j.jnoncrysol.2024.123130.

18. L. K. Varga and G. Kovacs, “Effect of Transversal Applied Bias Field on the Longitudinal Soft Magnetic Properties of Nanocrystalline Finemet Cores,” *IEEE Transactions on Magnetics* 48, no. 4 (2012): 1360–1362, https://doi.org/10.1109/TMAG.2011.2173321.

19. D. Azuma, N. Ito, and M. Ohta, “Recent Progress in Fe-Based Amorphous and Nanocrystalline Soft Magnetic Materials,” *Journal of Magnetism and Magnetic Materials* 501 (2020): 166373, https://doi.org/10.1016/j.jmmm.2019.166373.

20. M. J. Cai, J. J. Wang, Q. Q. Wang, et al., “Improvement of Soft-Magnetic Properties for Fe-Based Amorphous Alloys With High Saturation Polarization by Stress Annealing,” *Materials Research Letters* 11, no. 7 (2023): 595–603, https://doi.org/10.1080/21663831.2023.2199044.

21. N. M. Bruno, N. A. Adoo, E. Meakins, V. Keylin, G. E. Feichter, and R. D. Noebe, “The Effect of Stress-Annealing on the Mechanical and Magnetic Properties of Several Fe-Based Metal-Amorphous Nano-Composite Soft Magnetic Alloys,” *Journal of Non-Crystalline Solids* 600 (2023): 122037, https://doi.org/10.1016/j.jnoncrysol.2022.122037.

22. F. Zhu, J. C. Zhang, O. Demidenko, H. B. Sun, C. Wang, and J. H. Wang, “Influence of Stress-Induced Anisotropy on Domain Structure and Magnetic Properties of Fe-Based Nanocrystalline Alloy Under Continuous Tension Annealing,” *Journal of Non-Crystalline Solids* 600 (2023): 122035, https://doi.org/10.1016/j.jnoncrysol.2022.122035.

23. W. F. Zhang, J. F. Wang, C. Sun, T. Zhang, X. Y. Zhang, and T. Zhang, “Effect of Continuous Stress-Annealing on the Structure and Magnetic Properties of $Fe_{72.9}Si_{15.8}B_{6.9}Nb_{3.2}Cu_1Co_{0.2}$ Amorphous Alloy,” *Metals and Materials International* 29, no. 10 (2023): 3093–3101, https://doi.org/10.1007/s12540-023-01416-8.

24. L. Kraus, J. Bydžovský, and P. Švec, “Continuous Stress Annealing of Amorphous Ribbons for Strain Sensing Applications,” *Sensors and Actuators A: Physical* 106, no. 1 (2003): 117–120, https://doi.org/10.1016/S0924-4247(03)00147-X.

25. Z. J. Guo, X. X. Yang, M. J. Cai, et al., “Modulation of Magnetic Anisotropyand High-Frequency Soft-Magnetic Property of FeSiBNbCu Nanocrystalline Alloy via Continuous Tension Annealing,” *Scientia Sinica Physica, Mechanica & Astronomica* 55, no. 8 (2025): 286118, https://doi.org/10.1360/SSPMA-2024-0415.

26. B. W. Miao, Q. Luo, C. T. Chang, T. Liu, Y. Zhang, and J. Shen, “Effect of Co Addition and Annealing Conditions on the Magnetic Properties of Nanocrystalline FeCoSiBPCu Ribbons,” *Journal of Magnetism and Magnetic Materials* 477 (2019): 156–161, https://doi.org/10.1016/j.jmmm.2019.01.052.

27. J. W. Yao, C. Y. Zhao, S. H. Lv, et al., “Structural Relaxation and Magnetic Properties of Multicomponent Fe-Based Amorphous Alloy Ribbons,” *Rare Metals* (2025), https://doi.org/10.1007/s12598-025-03652-w.

28. K. Narita, J. Yamasaki, and H. Fukunaga, “Composition Dependence of Magnetic Moment and Curie Temperature in Amorphous $(Fe_xCo_{100-x})_{100-(y+z)}Si_yB_z$ Ribbons,” *IEEE Transactions on Magnetics* 14, no. 5 (1978): 1016–1018, https://doi.org/10.1109/TMAG.1978.1059981.

29. J. L. Jia, Y. Wu, L. X. Shi, et al., “Influence of Annealing Process on Soft Magnetic Properties of Fe-B-C-Si-P Amorphous Alloys,” *Materials* 17, no. 6 (2024): 1447, https://doi.org/10.3390/ma17061447.

30. J. C. Ye, J. Lu, C. T. Liu, Q. Wang, and Y. Yang, “Atomistic Free-Volume Zones and Inelastic Deformation of Metallic Glasses,” *Nature Materials* 9, no. 8 (2010): 619–623, https://doi.org/10.1038/nmat2802.

31. M. T. Sandor, H. B. Ke, W. H. Wang, and Y. Wu, “Anelasticity-Induced Increase of the Al-Centered Local Symmetry in the Metallic Glass $La_{50}Ni_{15}Al_{35}$,” *Journal of Physics: Condensed Matter* 25, no. 16 (2013): 165701, https://doi.org/10.1088/0953-8984/25/16/165701.

32. F. Mazaleyrat and R. Barrué, “Soft Amorphous and Nanocrystalline Magnetic Materials,” in *Handbook of Advanced Electronic and Photonic Materials and Devices* ed. H. Singh Nalwa, (Academic Press, 2001), 59–102, https://doi.org/10.1016/B978-012513745-4/50052-4.

33. M. Zhao, J. Pang, Y. R. Zhang, et al., “Optimization of Crystallization, Microstructure and Soft Magnetic Properties of $(Fe_{0.83}B_{0.11}Si_{0.02}P_{0.03}C_{0.01})_{99.5}Cu_{0.5}$ Alloy by Rapid Annealing,” *Journal of Non-Crystalline Solids* 579 (2022): 121380, https://doi.org/10.1016/j.jnoncrysol.2021.121380.

34. X. S. Li, F. C. Su, J. Zhou, et al., “Ductile Fe-Based Amorphous Alloy With Excellent Soft Magnetic Properties Induced by Low-Temperature Stress Annealing,” *Intermetallics* 166 (2024): 108201, https://doi.org/10.1016/j.intermet.2024.108201.

35. L. Zhu, S. S. Jiang, Z. Z. Yang, G. B. Han, S. S. Yan, and Y. G. Wang, “Magnetic Properties of a Fe-Based Amorphous Alloy With Stress Gradient,” *Journal of Magnetism and Magnetic Materials* 519 (2021): 167513, https://doi.org/10.1016/j.jmmm.2020.167513.

36. A. Williams, V. Moruzzi, A. Malozemoff, and K. Terakura, “Generalized Slater-Pauling Curve for Transition-Metal Magnets,” *IEEE Transactions on Magnetics* 19, no. 5 (1983): 1983–1988, https://doi.org/10.1109/TMAG.1983.1062706.

37. K. A. Gallagher, M. A. Willard, V. N. Zabenkin, D. E. Laughlin, and M. E. McHenry, “Distributed Exchange Interactions and Temperature Dependent Magnetization in Amorphous $Fe_{88-x}Co_xZr_7B_4Cu_1$ Alloys,” *Journal of Applied Physics* 85, no. 8 (1999): 5130–5132, https://doi.org/10.1063/1.369100.

38. T. Warski, P. Wlodarczyk, M. Polak, et al., “Influence of Cu Content on Structure and Magnetic Properties in $Fe_{86-x}Cu_xB_{14}$ Alloys,” *Materials* 13, no. 6 (2020): 1451, https://doi.org/10.3390/ma13061451.

39. X. D. Fan, H. Men, A. B. Ma, and B. L. Shen, “Soft Magnetic Properties in $Fe_{84-x}B_{10}C_6Cu_x$ Nanocrystalline Alloys,” *Journal of Magnetism and Magnetic Materials* 326 (2013): 22–27, https://doi.org/10.1016/j.jmmm.2012.08.045.

40. Z. Z. Li, S. X. Zhou, G. Q. Zhang, and W. Zheng, “Highly Ductile and Ultra-Thick P-Doped FeSiB Amorphous Alloys With Excellent Soft Magnetic Properties,” *Materials* 11, no. 7 (2018): 1148, https://doi.org/10.3390/ma11071148.

41. T. S. Chin, C. K. Chao, C. Y. Lin, et al., “Novel Tin-Containing Fe-Base Glassy Alloys,” *IEEE Transactions on Magnetics* 39, no. 5 (2003): 3016–3018, https://doi.org/10.1109/TMAG.2003.815876.

42. L. Hawelek, T. Warski, P. Włodarczyk, et al., “The Structure and Magnetic Properties of Rapidly Quenched $Fe_{72}Ni_8Nb_4Si_2B_{14}$ Alloy,” *Materials* 14, no. 1 (2020): 5, https://doi.org/10.3390/ma14010005.

43. A. Makino, T. Hatanai, A. Inoue, and T. Masumoto, “Nanocrystalline Soft Magnetic Fe-M-B (M = Zr, Hf, Nb) Alloys and Their Applications,” *Materials Science and Engineering: A* 226–228 (1997): 594–602, https://doi.org/10.1016/S0921-5093(96)10693-6.

44. T. Mizushima, A. Makino, S. Yoshida, and A. Inoue, “Low Core Losses and Soft Magnetic Properties of Fe-Al-Ga-P-C-B-Si Glassy Alloy Ribbons With Large Thicknesses,” *Journal of Applied Physics* 85, no. 8 (1999): 4418–4420, https://doi.org/10.1063/1.369803.

45. K. Takenaka, M. Nishijima, and A. Makino, “Effect of Metalloid Elements on the Structures and Soft Magnetic Properties in $Fe_{85.2}Si_xB_{14-x-y}P_yCu_{0.8}$ Alloys,” *IEEE Transactions on Magnetics* 50, no. 4 (2014): 2004704, https://doi.org/10.1109/TMAG.2013.2291396.

46. J. H. Zhang, F. P. Wan, Y. C. Li, et al., “Effect of Surface Crystallization on Magnetic Properties of $Fe_{82}Cu_1Si_4B_{11.5}Nb_{1.5}$ Nanocrystalline Alloy Ribbons,” *Journal of Magnetism and Magnetic Materials* 438 (2017): 126–131, https://doi.org/10.1016/j.jmmm.2017.04.086.

47. S. Mallick, P. Sharma, K. Takenaka, A. Makino, and S. Bedanta, “Static and Dynamic Behavior of Domain Walls in High B_s Soft Magnetic Ribbons Tuned by the Annealing Temperature,” *Journal of Physics D: Applied Physics* 51, no. 6 (2018): 065007, https://doi.org/10.1088/1361-6463/aaa43d.

48. M. Ohnuma, G. Herzer, P. Kozikowski, C. Polak, V. Budinsky, and S. Koppoju, “Structural Anisotropy of Amorphous Alloys With Creep-Induced Magnetic Anisotropy,” *Acta Materialia* 60, no. 3 (2012): 1278–1286, https://doi.org/10.1016/j.actamat.2011.11.017.

49. Q. Ding, J. W. Li, R. H. Zhang, et al., “Effect of Transverse Magnetic Field Annealing on the Magnetic Properties and Microstructure of FeSiBNbCuP Nanocrystalline Alloys,” *Journal of Magnetism and Magnetic Materials* 560 (2022): 169628, https://doi.org/10.1016/j.jmmm.2022.169628.

50. S. Flohrer, R. Schäfer, J. McCord, et al., “Dynamic Magnetization Process of Nanocrystalline Tape Wound Cores With Transverse Field-Induced Anisotropy,” *Acta Materialia* 54, no. 18 (2006): 4693–4698, https://doi.org/10.1016/j.actamat.2006.04.040.

51. R. Feng, Z. Y. Zhang, C. H. Chen, B. L. Shang, D. M. Li, and P. Yu, “Microstructure and Electrical Properties of Ni-Fe-B-Si-P Amorphous Alloys Controlled by Supercooled Liquid-Phase Annealing,” *Acta Physica Sinica* 74, no. 11 (2025): 116101, https://doi.org/10.7498/aps.74.20250368.

52. Z. T. Wang, J. Pan, Y. Li, and C. A. Schuh, “Densification and Strain Hardening of a Metallic Glass Under Tension at Room Temperature,” *Physical Review Letters* 111, no. 13 (2013): 135504, https://doi.org/10.1103/PhysRevLett.111.135504.

53. J. S. Blázquez, J. Marcin, F. Andrejka, V. Franco, A. Conde, and I. Skorvanek, “Anisotropy Field Distribution in Soft Magnetic Hitperm Alloys Submitted to Different Field Annealing Processes,” *Journal of Alloys and Compounds* 658 (2016): 367–371, https://doi.org/10.1016/j.jallcom.2015.10.210.

54. H. B. Sun, H. H. Huan, C. Wang, J. C. Zhang, and J. H. Wang, “Magnetic Properties, Anisotropy, and Domain Structure of Fe-Based Nanocrystalline Alloy Induced by Continuous stress-annealing Treatment,” *Journal of Magnetism and Magnetic Materials* 569 (2023): 170430, https://doi.org/10.1016/j.jmmm.2023.170430.

55. S. Chikazumi and J. C. D. Graham, *Physics of Ferromagnetism* (Oxford University Press, 1997), https://doi.org/10.1093/oso/9780198517764.001.0001.

56. J. Stöhr and H. C. Siegmann, *Magnetism: From Fundamentals to Nanoscale Dynamics* (Springer, 2006).

57. Y. H. Sun, A. Concustell, and A. L. Greer, “Thermomechanical Processing of Metallic Glasses: Extending the Range of the Glassy State,” *Nature Reviews Materials* 1, no. 9 (2016): 16039, https://doi.org/10.1038/natrevmats.2016.39.

58. P. Kozikowski, M. Ohnuma, R. Hashimoto, et al., “Temperature Memory Effect of Stress Annealing-Induced Anisotropy in Metallic Glasses,” *Physical Review Materials* 4, no. 9 (2020): 095604, https://doi.org/10.1103/PhysRevMaterials.4.095604.

59. F. Hu, Q. Luo, M. J. Cai, et al., “Transformation-Mediated and Relaxation-Assisted Macroscopic Tensile Plasticity With Strain-Hardening in Metallic Glass,” *Nature Communications* 16, no. 1 (2025): 10147, https://doi.org/10.1038/s41467-025-65120-4.

Supporting Information

Additional supporting information can be found online in the Supporting Information section.
Supporting Information S1: rar270252-sup-0001-suppl-data.docx.